



OPEN

Vibration mitigation of an MDoF system subjected to stochastic loading by means of hysteretic nonlinear locally resonant metamaterials

Francesco Basone^{1,2}, Oreste S. Bursi²✉, Fabrizio Aloschi^{2,3} & Günter Fischbach³

In this paper, we intend to mitigate absolute accelerations and displacements in the low-frequency regime of multiple-degrees-of-freedom fuel storage tanks subjected to stochastic seismic excitations. Therefore, we propose to optimize a finite locally resonant metafoundation equipped with massive resonators and fully nonlinear hysteretic devices. The optimization process takes into account the stochastic nature of seismic records in the stationary frequency domain; the records are modelled with the power spectral density S_0 and modified with a Kanai–Tajimi filter. Moreover, the massive superstructure of a fuel storage tank is also considered in the optimization procedure. To optimize the nonlinear behaviour of dampers, we use a Bouc–Wen hysteretic model; the relevant nonlinear differential equations are reduced to a system of linear equations through the stochastic equivalent linearization technique. The optimized system is successively verified against natural seismic records by means of nonlinear transient time history analyses. Finally, we determine the dispersion relations for the relevant periodic metafoundation.

Within linear metamaterials, a new category of applications of phononic—or periodic—structures as alternatives to classic seismic isolators for earthquake mitigation has received growing interest^{1–4}. The increasing popularity of these structures resides in the possibility of exploiting the advantages of locally resonant acoustic metamaterials (LRAMs) due to their ability to attenuate low-frequency waves by means of unit cells much smaller than the seismic wavelength of the desired frequency region. The most common isolation solutions use lead-rubber bearings or spherical bearing devices, which are quite effective for the horizontal components of earthquakes. Nonetheless, these solutions require two strong floors, exert a very high stiffness against the vertical component of an earthquake, and are quite ineffective for large structures subjected to rocking⁵. To reduce the seismic responses of superstructures, Cheng and Shi³ and Casablanca et al.⁴ studied periodic and finite locally resonant foundations. Although good response reduction results were obtained, neither of the proposed periodic systems were designed for gravity and/or seismic load combinations. Furthermore, the authors did not consider the feedback forces from the superstructures to the metafoundations. To overcome these drawbacks, we proposed a finite lattice LRAM, the so-called metafoundation, for the seismic protection of multiple-degrees-of-freedom (MDoF) systems, i.e., storage tanks^{2,6,7}. The relevant coupled metafoundation-tank system is depicted in Fig. 1a.

The foundation consists of flexible steel columns and concrete slabs that define the primary load-bearing structure, while massive concrete masses are considered resonators. The construction site is Priolo Gargallo in Sicily, Italy. The site is characterized by a peak ground acceleration (PGA) of 0.56 g for a return period $T_R = 2475$ years. Therefore, a linear elastic design according to the Italian code⁸ was carried out; the resulting minimal column stiffnesses allow the metafoundation to remain undamaged following safe shutdown earthquakes (SSEs). As a result, the columns have a total height of 4 m with hollow cross-sectional dimensions of 300 × 300 mm and a thickness of 30 mm. A 3D sketch of the coupled metafoundation-tank system shows that the foundation structure is composed of a finite number of 9-unit cells. Square hollow-section steel columns

¹Engineering and Architecture Faculty, University of Enna “Kore”, Viale delle Olimpiadi, 94100 Enna, Italy. ²Department of Civil, Environmental and Mechanical Engineering, University of Trento, Via Mesiano 77, 38123 Trento, Italy. ³IGF - Ingenieurgesellschaft Dr. Ing. Fischbach mbH, An der Vogelrute 2, 50374 Erftstadt-Lechenich, Germany. ✉email: oreste.bursi@unitn.it

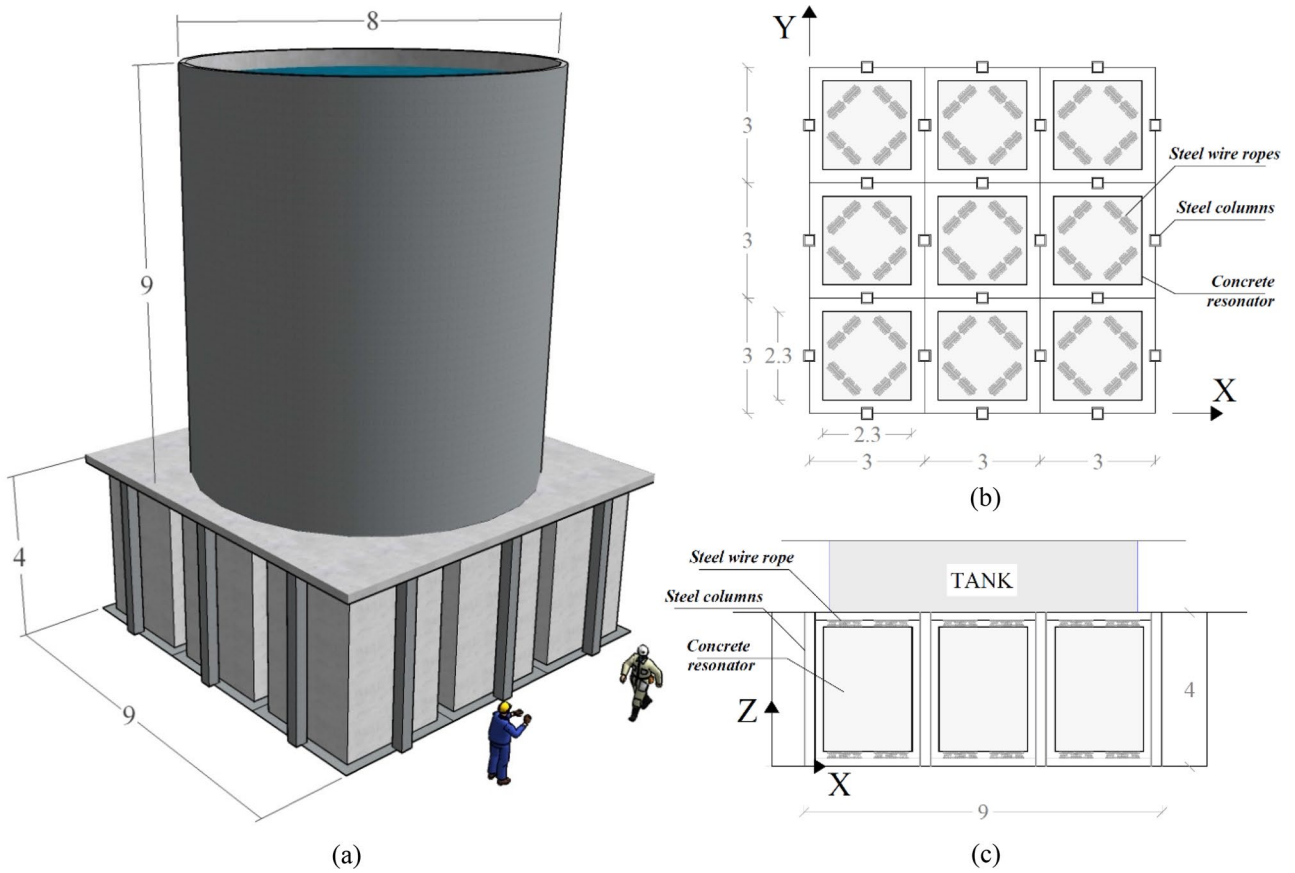


Figure 1. Coupled foundation—tank system: (a) 3D view, (b) layout of the unit cells and (c) cross section of the metafoundation. Dimensions are in m.

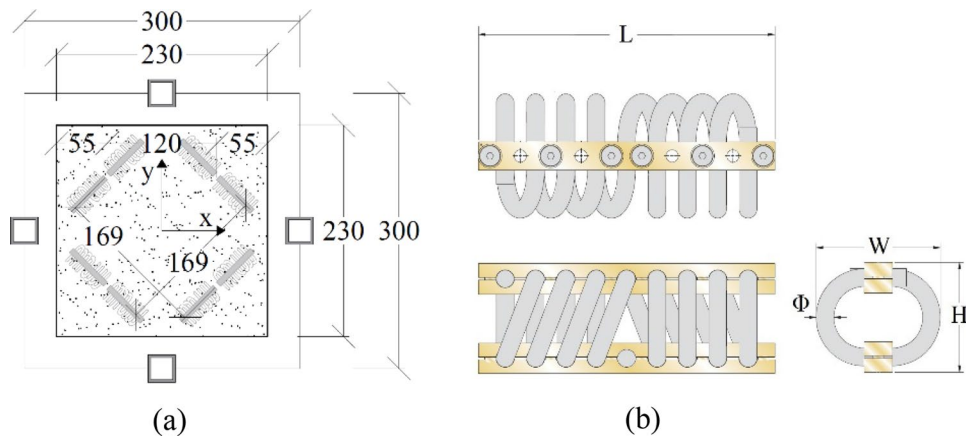


Figure 2. (a) Configuration of a single unit cell equipped with steel wire ropes; (b) details of a single wire rope. Dimensions are in cm.

support the concrete slab and provide the lateral stiffness of the metafoundation. Each unit cell includes a massive concrete cube linked to the foundation (see Fig. 1b, c) by means of wire ropes, as depicted in Fig. 2.

Nonetheless, two basic issues remain unresolved: the optimization of structural devices, i.e., springs and/or dampers, operating in the nonlinear regime within finite lattices and the inclusion of the stochastic nature of the seismic input characterized by a large random uncertainty.

With regard to the first issue, i.e., the selection of proper hysteretic dampers, Basone et al.⁶ suggested the use of wire ropes, which are simple devices able to both effectively suspend the concrete resonators inside the foundation and allow motion in all three main directions. Therefore, the behaviour of wire ropes is quite complex,

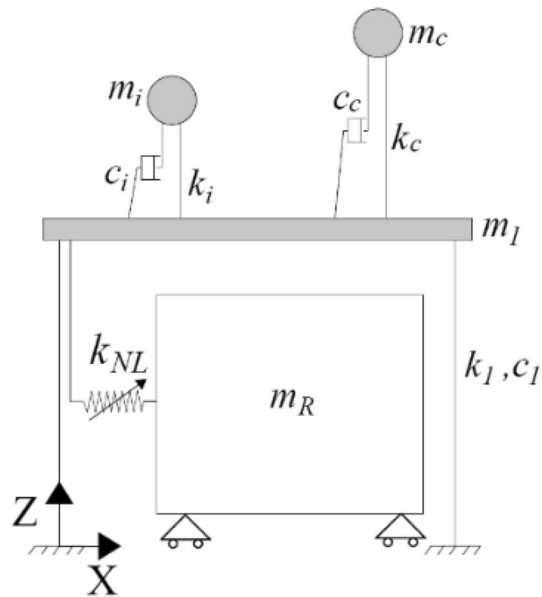


Figure 3. Metafoundation-tank coupled system model: condensed mass system (CMS).

and the characterization of their nonlinear properties is difficult^{9,10}. More precisely, the mechanical flexibility of wire ropes provides good isolation properties, and the sliding friction between the intertwined cables results in high dissipative capabilities. As a result, these devices can achieve equivalent damping ratios of 15–20% with low production and maintenance costs. Their hysteretic behaviour can be reproduced with the well-known Bouc–Wen model^{9–11}. This model is quite popular because it can describe the behaviour of a nonlinear hysteretic system with a compact first-order differential equation¹².

If we consider the aforementioned devices in periodic systems, the analysis of nonlinear metamaterials is still very challenging^{13,14}. For instance, from a perturbation approach specifically applied to weakly nonlinear periodic chains¹⁵, the following topics emerge: (1) the solutions to the nonlinear wave equations are amplitude dependent; (2) the wave amplitudes influence their own propagation characteristics, the so-called self-action; and (3) the analysis methods in the presence of self-action often do not trace all solutions when more than one dominant component is involved. Nonetheless, several researchers have devoted considerable effort to improving our understanding of nonlinear metamaterial-based systems. For instance, to reduce wave transmission in both ultralow and ultrabroad bands with band gaps and chaotic bands, Fang et al.¹⁶ developed both a theoretical approach and an experimental validation to conceive nonlinear acoustic metamaterials (NAMs). Based on a new mechanism for wave mitigation and control consisting of the nonlinear interaction between propagating and evanescent waves, Zega et al.¹⁷ recently presented experimental proof of the appearance of a subharmonic transmission attenuation zone due to an energy exchange induced by autoparametric resonance. In contrast, Gupta et al.¹⁸ explored a wide range of nonlinear mechanical behaviours that can be generated from the same lattice material by changing the building block into a dome-shaped structure. In particular, they proposed a novel hourglass-shaped lattice metastructure that takes advantage of the combination of two oppositely oriented coaxial domes.

With regard to the second issue, i.e., the stochastic nature of the seismic input and the subsequent stochastic response analysis of hysteretic systems, an abundance of literature is available^{12,19,20}. In this respect, the equivalent (stochastic) linearization technique (ELT)^{12,19}, based on a non-Gaussian probability density function, is viable because it can be extended (in a relatively straightforward manner) to MDoF systems. Socha and Pawleta²¹ discussed the advantages and disadvantages of this technique.

In summary, to achieve the best performance of a finite locally resonant metafoundation, the following objectives are pursued hereinafter: (1) the optimization of the nonlinear behaviour of wire ropes reproduced with hysteretic Bouc–Wen models and (2) the application of the ELT to fully nonlinear devices taking into account the stochastic nature of the seismic input in both the frequency domain and the time domain.

The superstructure is composed of a slender fuel storage tank and its equivalent 2D lumped mass model²² (see Figs. 1a and 3). More precisely, the slender tank was part of an existing plant, i.e., tank #23 or #24 of Case Study #1, analysed in a European research project^{2,7}. Housner's model²³ is adopted to simulate the hydrodynamic response of liquid containers. This model allows us to associate the inertial force of the liquid with two different masses: the impulsive mass and the convective mass. The tank response is reduced to the contributions of the two main impulsive and convective modes, and the tank wall thickness is taken into account. The tank's liquid content exhibits axial symmetry, which is sufficient to analyse the dynamics in one direction. However, each resonator can vibrate in all three (X, Y and Z) directions.

With regard to the metafoundation, it is designed to remain undamaged for an active seismic site located in Priolo Gargallo, Italy. Considering a consistent seismic input for linear/nonlinear time history analyses, a set of

natural earthquakes that correspond to SSE events are selected from Italian and European databases and fitted on average to the uniform hazard spectrum (UHS) of Priolo Gargallo.

To take the stochastic nature of the seismic input into account, the computations are carried out in the frequency domain, and because the analysis of nonlinear periodic systems entails the aforementioned difficulties¹⁵, the ELT is adopted for the Bouc–Wen model. Therefore, an average power spectral density (PSD) function of the accelerograms is evaluated. The resulting PSD function is filtered with a Kanai–Tajimi filter²⁴ modified by Clough and Penzien²⁵ and subsequently adopted in the optimization procedure. The resulting optimized meta-foundation is then verified through nonlinear time history analyses (THAs) of the coupled system subjected to the aforementioned ground motions.

Methods

Nonlinear metafoundation system modelling. To address simpler coupled systems and to benefit from the optimization considering different stiffness and damping values, the condensed mass system (CMS) shown in Fig. 3 is considered. Through an exact dynamic condensation of both the masses and stiffnesses along X and Y directions we can analyse the CMS as a 2D system. This dynamic condensation does not lead to errors since all resonators in both the X and the Y directions are assumed to be endowed with the same mass and stiffness (see Fig. 1b). The CMS is depicted in Fig. 3, in which the dynamic characteristics of the system are reported as well. Herein, m_p , c_i and k_i represent the mass, stiffness and damping coefficients, respectively, of the impulsive mass of the superstructure-tank system, while m_c , c_c and k_c represent the mass, stiffness and damping coefficients of the relevant convective mass.

The following system of equations of motion (EOMs) describes the dynamics of the aforementioned meta-foundation-tank coupled system:

$$\mathbf{M} \ddot{\mathbf{R}}(t) + \mathbf{C} \dot{\mathbf{u}}(t) + \mathbf{K} \mathbf{u}(t) + u_y \mathbf{K}^{\text{NL}} \mathbf{z}(t) = \mathbf{F}(t) \quad (1)$$

where \mathbf{M} , \mathbf{C} and \mathbf{K} are the mass, damping and stiffness matrices, respectively; \mathbf{K}^{NL} defines the component of the stiffness matrix that contains the terms $(1 - \alpha_n) k_n$ introduced later; $\mathbf{z}(t)$ defines the vector that contains the components $z_n(t)$ of the n th resonator modelled in the next subsection; and u_y sets the yielding displacement of the device. Therefore, Eq. (1) is a nonlinear system of EOMs due to the presence of $u_y \mathbf{K}^{\text{NL}} \mathbf{z}(t)$. The vector $\mathbf{u}(t)$ indicates the displacement vector, whilst single and double dots represent single and double derivatives with respect to (w.r.t.) time, respectively. Furthermore, $\mathbf{F}(t) = -\mathbf{M} \boldsymbol{\tau} \ddot{u}_g(t)$ represents the forcing vector, where $\boldsymbol{\tau}$ is the mass influence vector and $\ddot{u}_g(t)$ represents the ground acceleration.

To evaluate the dynamic properties of the CMS, the system equivalent reduction expansion procedure (SEREP) is adopted. This method allows the modal vectors of the CMS to be reduced²⁶, therefore, the convective mode and the relevant DoFs of the tank can be eliminated from the full set of n DoFs, while the effects on the lower a modes can be retained. More precisely, the SEREP technique is based on the following transformation:

$$\mathbf{u}_n = \mathbf{T} \mathbf{u}_a \quad (2)$$

where $\mathbf{T} = \Phi_n \Phi_a^g$ is the transformation matrix, Φ_n is the modal matrix of the original system, and Φ_a^g is the generalized inverse of the modal matrix of the active/reduced system. More precisely, Φ_a^g can be evaluated as

$$\Phi_a^g = \left(\Phi_a^T \Phi_a \right)^{-1} \Phi_a^T \quad (3)$$

As a result, the system matrices of the reduced system are $\tilde{\mathbf{M}} = \mathbf{T}^T \mathbf{M} \mathbf{T}$, $\tilde{\mathbf{K}} = \mathbf{T}^T \mathbf{K} \mathbf{T}$ and $\tilde{\mathbf{C}} = \mathbf{T}^T \mathbf{C} \mathbf{T}$, while the forcing term becomes $\tilde{\mathbf{F}} = -\mathbf{T}^T \mathbf{M} \boldsymbol{\tau} \ddot{u}_g$. Since the optimization procedure requires an inversion of the transmission matrix \mathbf{T} for each frequency interval, the SEREP technique also contributes to the reduction in the run time of the optimization algorithm.

Modelling of nonlinear devices. The nonlinear devices utilized in this work are steel wire ropes, schematically depicted in Fig. 2b. Steel wire ropes are a commonly used solution in seismic engineering due to their dissipative behaviour. Moreover, they represent an inexpensive solution in terms of both production and maintenance costs. Thus, many researchers have investigated the hysteretic characteristics of wire ropes when subjected to shear forces^{9–11}. In this context, steel wire ropes have already been successfully utilized in metafoundations. In some research works^{6,27}, the goal was the protection of tanks against both horizontal and vertical ground accelerations by means of finite lattices equipped with nonlinear devices endowed with significant flexibility and hysteretic damping. Furthermore, steel wire ropes allow effective motion of the resonators along X, Y and Z directions, which can be easily deduced by Fig. 1.

To model the nonlinear dissipative behaviour of wire ropes, we employ the Bouc–Wen model. This model has been adopted to capture the hysteretic behaviours of many other seismic devices^{9,10,28}.

For the sake of clarity, let us consider a single-degree-of-freedom (SDoF) system:

$$m \ddot{u}(t) + c \dot{u}(t) + R(t) = F(t) \quad (4)$$

where $R(t)$ defines the nonlinear restoring force:

$$R(t) = \alpha k u(t) + (1 - \alpha) k u_y z(t) \quad (5)$$

Geometric characteristics				Parameters of the Bouc–Wen model					
H [mm]	W [mm]	L [mm]	Φ [mm]	k_0 [kN/mm]	R_y [kN]	u_y [mm]	n [-]	A [-]	α [-]
178	216	520.7	26.6	1.35	2.97	2.2	1.0	1.0	0.254

Table 1. Geometric and mechanical properties of the wire ropes.

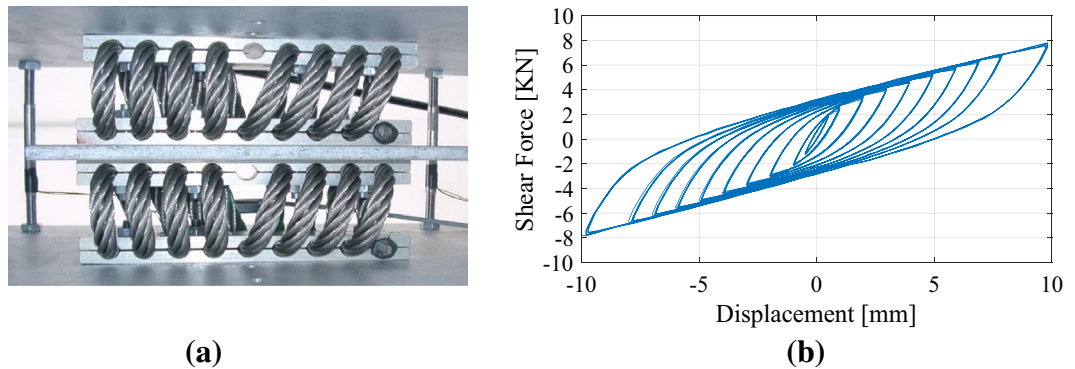


Figure 4. (a) Two wire ropes with a central plate subjected to simple shear; (b) hysteric response of the wire rope under cyclic shear loading after Paolacci and Giannini⁹.

where k represents the yielding stiffness and u_y is the yielding displacement. The z term is a dimensionless hysteric component provided by the solution of the following nonlinear differential equation that contains three state variables:

$$\dot{z}(t) = u_y^{-1} [A\dot{u}(t) - \gamma|\dot{u}(t)||z(t)|^{n-1}z(t) - \beta\dot{u}(t)|z(t)|^n] \quad (6)$$

The shape and smoothness of each hysteric loop is controlled by the parameters A , β , γ and n . Moreover, the term $\alpha = k_p/k_0$ in Eq. (5) defines the ratio of the postyielding stiffness to the preyielding stiffness, with

$$k_0 = \left(\frac{\partial R(u, \dot{u}, z)}{\partial u} \right)_{z=0} = \alpha k + (1 - \alpha)kA; \quad k_p = \left(\frac{\partial R(u, \dot{u}, z)}{\partial u} \right)_{z=z_{max}} = \alpha k_0 \quad (7)$$

and $z_{max} = [A/(\beta + \gamma)]^{1/n}$.

Suitable values of A , β , γ and n govern the hardening or softening nonlinearities in the Bouc–Wen model. For instance, with $|\gamma| > |\beta|$, $\gamma < 0$, a hardening behaviour is obtained. Moreover, the elastoplastic hysteresis case is approached when $n \rightarrow \infty$, where n modulates the sharpness of the yield. A choice of $n = 1$ entails a closed-form solution of Eq. (6) with simple exponential functions²⁸.

To identify the relevant mechanical characteristics, Paolacci and Giannini carried out an ad hoc experimental campaign⁹. On that database, we initialize the main parameters of the Bouc–Wen model. We select wire rope WR36-400-08, whose geometric dimensions are described in Table 1. In particular, k_0 is the initial shear stiffness, and R_y represents the vertical load-bearing capacity. The authors⁹ found $\alpha = 0.254$ and $u_y = 2.2$ mm.

For the sake of clarity, two coupled wire ropes can be observed in the test rig of Fig. 4a; this arrangement allows cyclic simple shear tests to be reproduced by means of a central plate⁹. The corresponding hysteric response is depicted in Fig. 4b.

A generic cycle of the Bouc–Wen model is shown in Fig. 5a with the main mechanical and kinematic parameters. A careful reader will notice that this model is symmetric, as can be understood from Eq. (6); nonetheless, this property does not limit its capability to properly trace the experimental response depicted both in Figs. 4b and 5b.

Note that after choosing steel wire rope, the Bouc–Wen model parameters A and $(\beta + \gamma)$ can be functionally selected to be $A = 1$ and $\beta + \gamma = 1$. As shown by Constantinou and Adnane²⁹, this choice leads to the collapse of the model to Ozdemir's model, which is a rate-dependent Maxwell model with a nonlinear dashpot. By setting $A = 1$ in Eq. (7), indeed, the value of the initial stiffness $k = R_y/u_y = k_0$ is retrieved; then, by setting $\beta + \gamma = 1$, the maximum strength factor z_{max} in Eq. (6) becomes $z_{max} = [A/(\beta + \gamma)]^{1/n} = 1$ with $z \in [-1, 1]$.

Seismic input model. Given the epistemic and mainly aleatoric uncertainties of the seismic input, it is not feasible to optimize a system endowed with nonlinear devices on a conventional time basis. A more accurate probabilistic (stochastic) approach is required in which both the excitation and the response are described in terms of statistical parameters such as the mean square and the variance of the vibration amplitudes. As a result, our approach relies heavily on random vibrations treated in the frequency domain, and stochastic linearization carried out in the next subsection. Therefore, the input is assumed to be a weakly stationary Gaussian-filtered

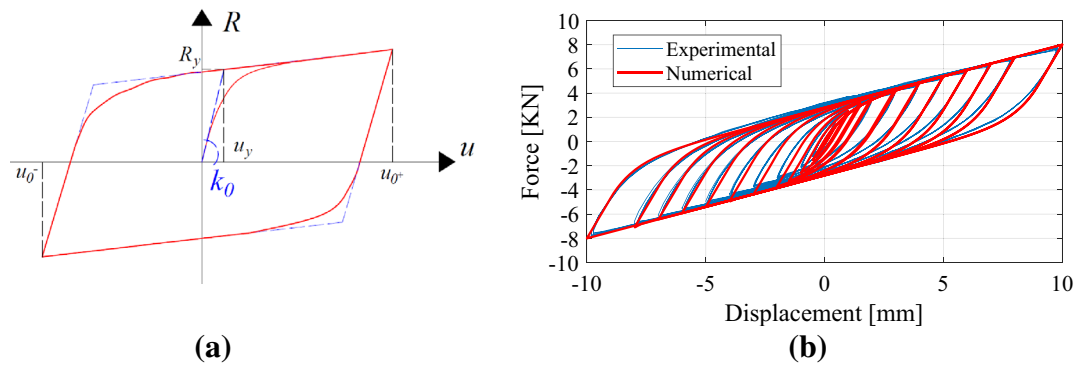


Figure 5. (a) Typical hysteretic loop of a Bouc–Wen model; (b) comparison between experimental and numerical responses after Paolacci and Giannini⁹.

Event	Country	R, distance [km]	M, magnitude
Victoria Mexico	Mexico	13.8	6.33
Loma Prieta	USA	3.85	6.93
Northridge-01	USA	20.11	6.69
Montenegro	Montenegro	25.00	6.90
Erzincan	Turkey	13.00	6.60
South Iceland	Island	7.00	6.50
L'Aquila Mainshock	Italy	4.87	6.30
Loma Prieta	USA	11.03	6.93
Landers	USA	11.03	7.28
South Iceland	Island	11.00	6.40
L'Aquila Mainshock	Italy	4.63	6.30
L'Aquila Mainshock	Italy	4.39	6.30

Table 2. Selected natural accelerograms.

white noise random process with zero mean and spectral intensity S_0 . Consequently, the soil is approximately taken into account by means of the Kanai–Tajimi filter²⁴, and to avoid unrealistic high values of the excitation in the low-frequency range, we utilize an additional filter suggested by Clough and Penzien²⁵. The result is the so-called Kanai–Tajimi Clough–Penzien (KTCP) filter, and the resulting PSD function is

$$S_{\ddot{u}_g}(\omega) = S_0 \frac{4\zeta_g^2 \omega_g^2 \omega^2 + \omega_g^4}{4\zeta_g^2 \omega_g^2 \omega^2 + (\omega_g^2 - \omega^2)^2} \frac{\omega^4}{4\zeta_f^2 \omega_f^2 \omega^2 + (\omega_f^2 - \omega^2)^2} \tag{8}$$

where $\omega_g = 14$ rad/s is the frequency associated with the ground and $\zeta_g = 0.6$ is the relevant damping ratio. The parameters $\omega_f = 0.75$ rad/s and $\zeta_f = 1.9$ are assumed for the low pass filter²⁵, whilst the PSD intensity $S_0 = 0.09$ m²/s³ for safe shutdown earthquakes (SSEs) corresponds to seismic activity with a return period of 2475 years. In the time domain, the KTCP filter becomes

$$\ddot{u}_g = \omega_g^2 u_g + 2\zeta_g \omega_g \dot{u}_g - \omega_f^2 u_f - 2\zeta_f \omega_f \dot{u}_f \tag{9}$$

where some variables can be treated in a state-space formulation:

$$\begin{aligned} \ddot{u}_g &= \mathbf{a}_f^T \mathbf{u}_f \\ \dot{u}_f &= \mathbf{A}_f \mathbf{u}_f + \mathbf{V}_f f(t) \end{aligned} \tag{10a}$$

$$\mathbf{u}_f = \begin{bmatrix} u_f \\ \dot{u}_f \\ u_g \\ \dot{u}_g \end{bmatrix}; \mathbf{a}_f = \begin{bmatrix} -\omega_f^2 \\ -2\zeta_f \omega_f \\ \omega_g^2 \\ -2\zeta_g \omega_g \end{bmatrix}; \mathbf{A}_f = \begin{bmatrix} 0 & 1 & 0 & 0 \\ -\omega_f^2 & -2\zeta_f \omega_f & \omega_g^2 & 2\zeta_g \omega_g \\ 0 & 0 & 0 & 1 \\ 0 & 0 & -\omega_g^2 & -2\zeta_g \omega_g \end{bmatrix}; \mathbf{V}_f = \begin{bmatrix} 0 \\ 0 \\ 0 \\ 1 \end{bmatrix} \tag{10b}$$

where $f(t)$ denotes the bedrock Gaussian zero-mean white noise process. Both the filter parameters and the PSD intensity S_0 are chosen to fit the stationary PSD spectra of 12 natural seismic records (see Table 2) selected from Italian and European databases with a 2% probability of exceedance in 50 years.

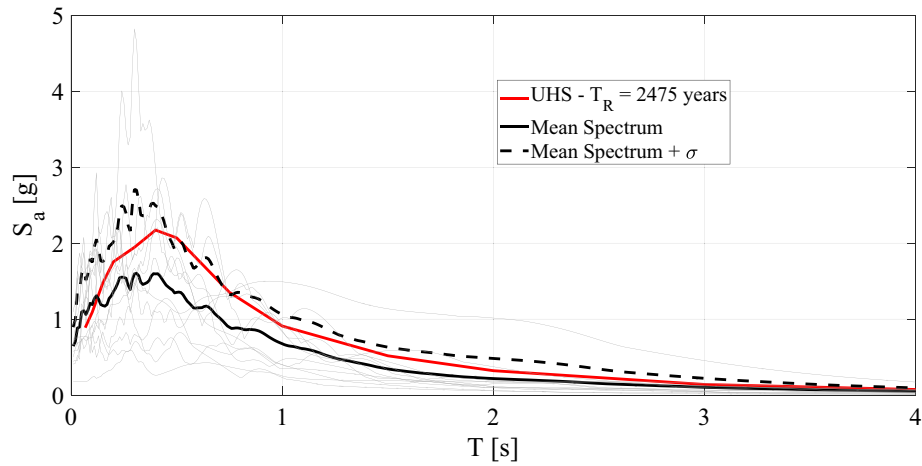


Figure 6. Response spectra of the selected accelerograms for SSEs; the UHS of Priolo Gargallo (Italy) is depicted in red.

The corresponding elastic response spectra, their mean and their mean plus one standard variation, together with the target uniform hazard spectrum (UHS) relevant to Priolo Gargallo, are plotted in Fig. 6. The twelve records collected in Table 2 are selected as follows. Let \mathbf{s}_0 be the target spectrum value vector, i.e., the mean or the mean plus one standard deviation, let \mathbf{S} be the spectra matrix of the n_a accelerograms, and let α be the vector of the $n_a \times 1$ selection coefficients α_i . We seek for the vector α that satisfies

$$\left\| \frac{1}{\sum_{i=1}^{n_a} \alpha_i} \mathbf{S} \alpha - \mathbf{s}_0 \right\|^2 = \min \tag{11}$$

where $0 \leq \alpha_i \leq 1$ and $\sum_{i=1}^{n_a} \alpha_i = n$.

Hence, the selection is performed with all possible combinations of the n accelerograms among a set of n_a records. Thus, we can easily take into account the dispersion of the records about the mean spectrum. The discrepancy between the maximum peak of the two spectra, i.e. the UHS and the Mean Spectrum + σ should entail limited effects on the responses of the nonlinear coupled systems presented in the section Results.

Equivalent linearization and optimization procedure. To model the wire ropes illustrated in Fig. 2b, which are not easily treated mathematically, we propose the stochastic linearization technique²¹. As a result, the treatment of the linearized metafoundation-tank coupled system allows the optimization procedure to be performed in the frequency domain and bypasses several difficulties related to the determination of the dispersion properties of fully nonlinear periodic systems¹⁵. With regard to the parameters to be optimized, to maximize antiresonance or negative effects, the masses of the resonators are set as the largest masses compatible with unit cell dimensions. Moreover, the other parameters are derived from construction or design constraints, e.g., the design column size and slab thickness; therefore, mainly the stiffness and damping of wire ropes, i.e., the relevant dissipated energy controlled by the parameters of Eqs. (5) and (6), can be optimized.

Since the system of EOMs in Eq. (1) characterizes a coupled nonlinear system, classic linear random vibration theory is not applicable. Therefore, to linearize the vector $\mathbf{u}_r \mathbf{K}^{NL} \mathbf{z}(t)$, we employ the ELT. For the sake of clarity, for an SDOF system with $N = 1$, Eq. (6) becomes

$$\dot{\mathbf{z}} + c_{eq} \dot{\mathbf{u}} + k_{eq} \mathbf{z} = 0 \tag{12}$$

where c_{eq} and k_{eq} are linearization coefficients that are “equivalent” in a statistical sense^{30,31}. At this stage, it is useful to introduce a state-space formulation of Eqs. (1) and (12):

$$\frac{d}{dt} \mathbf{Y} = \mathbf{G} \mathbf{Y} + \mathbf{V} f(t) \tag{13}$$

with

$$\mathbf{Y} = \begin{bmatrix} \mathbf{u} \\ \dot{\mathbf{u}} \\ \mathbf{z} \\ \mathbf{u}_f \end{bmatrix}; \mathbf{G} = \begin{bmatrix} \mathbf{0}_{N \times N} & \mathbf{I}_{N \times N} & \mathbf{0}_{N \times N} & \mathbf{0}_{N \times r} \\ -\mathbf{M}^{-1} \mathbf{K}^L & -\mathbf{M}^{-1} \mathbf{C} & -\mathbf{M}^{-1} \mathbf{K}^{NL} & -\mathbf{1} \mathbf{a}_f^T \\ \mathbf{0}_{N \times N} & -\mathbf{c}_{eq} & -\mathbf{k}_{eq} & \mathbf{0}_{N \times r} \\ \mathbf{0}_{r \times N} & \mathbf{0}_{r \times N} & \mathbf{0}_{r \times N} & \mathbf{A}_f \end{bmatrix}; \mathbf{V} = \begin{bmatrix} \mathbf{0}_{N \times 1} \\ \mathbf{0}_{N \times 1} \\ \mathbf{0}_{N \times 1} \\ \mathbf{V}_f \end{bmatrix} \tag{14}$$

where \mathbf{Y} is the state-space vector, \mathbf{K}^L and \mathbf{K}^{NL} define the linear and nonlinear components of the stiffness matrix, respectively, and \mathbf{k}_{eq} and \mathbf{c}_{eq} represent matrices including equivalent linear coefficients. Moreover, N defines the number of DoFs of the system, and $r=4$ defines the number of equations of the KTCP filter introduced in the previous subsection. Let the covariance matrix of \mathbf{Y} be \mathbf{S} with $S_{ij} = E[y_i y_j]$, and assume that the seismic input is stationary. The solution of Eq. (13) can be derived from the following Lyapunov system of equations:

$$\mathbf{G} \mathbf{S} + \mathbf{S} \mathbf{G}^T + \mathbf{B} = \mathbf{0} \tag{15}$$

where \mathbf{B} is a zero matrix except for the generic diagonal element corresponding to the nonzero row of the forcing function vector, i.e., $B_{ij} = 2\pi S_0$. Equation (15) is solved with the algorithm proposed by Bartels and Steward³². As expected, \mathbf{k}_{eq} and \mathbf{c}_{eq} are not known a priori; in this regard, Maldonado et al.³⁰ suggested setting the initial values for an iterative solution procedure $c_{eq} = 1$ and $k_{eq} = 0.05 (\beta + \gamma)$ for faster convergence. Further details about the whole procedure are available in Maldonado et al.³⁰ and Spanos et al.³¹.

To operate in the frequency domain, we start from Eq. (4) for a SDoF system and define the transfer function $\mathbf{H}(\omega)$ of the coupled system depicted in Fig. 3. However, Eq. (13) includes the KTCP filter, and the derivation is more burdensome for an MDoF system. Therefore, the relevant $\mathbf{H}(\omega)$ becomes

$$\mathbf{H}(\omega) = \left[-\omega^2 m + i\omega c + \alpha k - \frac{i\omega}{i\omega + k_{eq}} c_{eq} (1 - \alpha) k u_y \right]^{-1} \tag{16}$$

where the details of the derivation can be found in the Supplementary Material. Its generalization is expressed as

$$\mathbf{H}(\omega) = [-\omega^2 \mathbf{M} + i\omega \mathbf{C} + \mathbf{K} + \mathbf{K}^{eq}]^{-1} \tag{17}$$

where \mathbf{K}^{eq} contains zero terms except those in which the n th resonator is physically connected. More precisely, the nonzero terms k_{ij}^{eq} of matrix \mathbf{K}^{eq} are

$$k_{ij}^{eq} = -\frac{i\omega}{i\omega + k_{eq}} c_{eq} (1 - \alpha_n) u_y k_n \tag{18}$$

where α_n and k_n refer to the n th resonator of the metafoundation. Note that for $\alpha = 1$, the transmission matrix in Eq. (17) degenerates into a linear transmission matrix.

To carry out the optimization, we minimize the interstorey displacement and the absolute acceleration of the tank's impulsive mode, where the relevant variances σ_{dr} and σ_{acc} , respectively, are expressed as

$$\begin{aligned} \sigma_{dr}^2 &= \int_0^{+\infty} |H_{imp}(\omega) - H_{res}(\omega)|^2 S_{\ddot{u}_g}(\omega) d\omega \\ \sigma_{acc}^2 &= \int_0^{+\infty} |1 - \omega^2 H_{imp}(\omega)|^2 S_{\ddot{u}_g}(\omega) d\omega \end{aligned} \tag{19}$$

where $H_{imp}(\omega)$ defines the transfer function of the impulsive mass and $H_{res}(\omega)$ is the transfer function of the resonator's layer. The dimensionless performance indices are defined as follows:

$$\begin{aligned} PI_{dr} &= \frac{\sigma_{dr}^2}{\sigma_{dr, fixed}^2} \\ PI_{acc} &= \frac{\sigma_{acc}^2}{\sigma_{acc, fixed}^2} \end{aligned} \tag{20}$$

where $\sigma_{dr, fixed}^2$ and $\sigma_{acc, fixed}^2$ represent the variances of the interstorey drift and the absolute acceleration, respectively, w.r.t. a clamped tank.

The optimization procedure relies on the design variables $k_{k,n}$ and $\beta_{k,n}$ collected in the parameter vector \mathbf{X}^{NL} :

$$\mathbf{X}^{NL} = [k_{1,1}, k_{k,n}, A_{1,1}, A_{k,n}, \beta_{1,1}, \beta_{k,n}, \gamma_{1,1}, \gamma_{k,n}]^T \tag{21}$$

The statement of our optimization problem is as follows:

$$\min_{k,n} PI_{dr}(\mathbf{X}^{NL}) \text{ or } \min_{k,n} PI_{acc}(\mathbf{X}^{NL}) \tag{22}$$

where $k = (1, \dots, n_k)$ and $n = (1, \dots, n_r)$. The limits imposed on the design variable $\beta_{k,n}$ are

$$0 < \beta_{k,n} < 1 \tag{23}$$

Further details about the bound of Eq. (23) were already provided in the section [Modelling of nonlinear devices](#).

Dispersion characteristics of the linearized periodic system. Though the system is linearized by means of Eq. (12), the effects of the nonlinear devices depicted in Fig. 2 on the band structure of the relevant

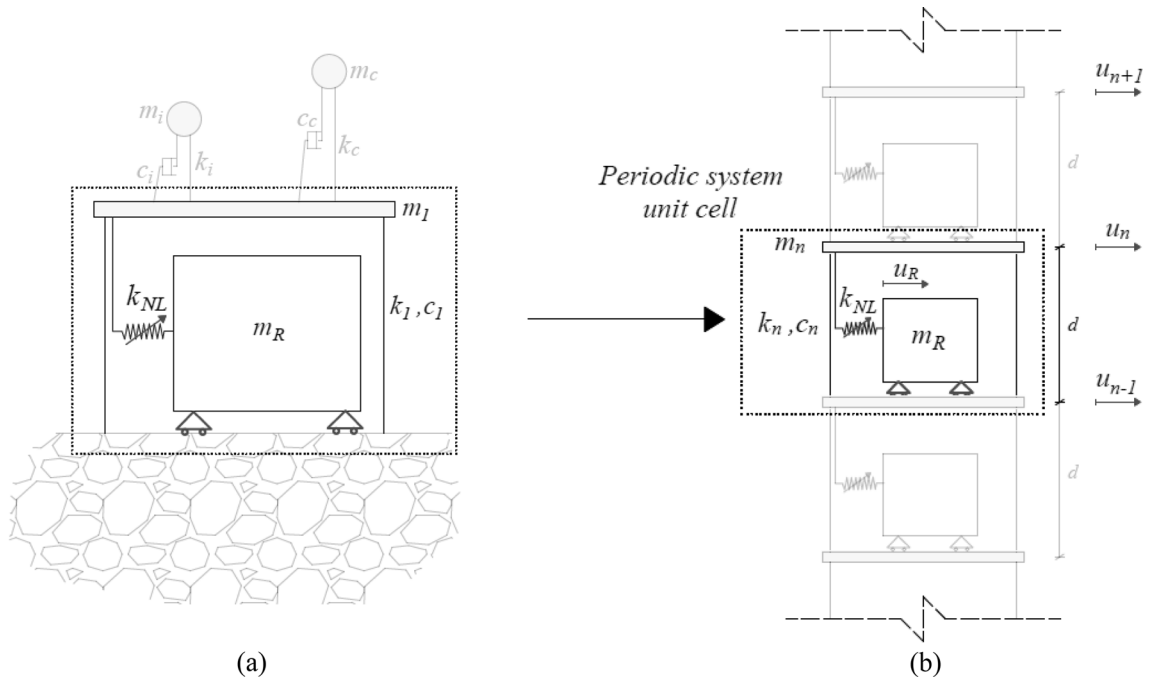


Figure 7. Dynamic systems: (a) coupled finite lattice metafoundation-tank system; (b) metafoundation modelled as a periodic system.

periodic system are of interest. On the one hand, we can observe the effect of equivalent damping on the dispersion relationships; on the other hand, we can appreciate the effects of the PSD S_0 .

First, let us consider Fig. 7, which shows both the finite lattice 1-layer structure (see Fig. 7a) and the relevant system of repetitive unit cells depicted in Fig. 7b.

The 2-DoF system associated with the unit cell, i.e., slab and resonator of Fig. 7b, can be represented as follows:

$$\begin{cases} m_n \ddot{u}_n + c_n(\dot{u}_n - \dot{u}_{n-1}) + c_n(\dot{u}_n - \dot{u}_{n+1}) + k_n(u_n - u_{n-1}) + k_n(u_n - u_{n+1}) - \alpha k_0(u_R - u_n) - (1 - \alpha)k_0 u_y z(t) = 0 \\ m_R \ddot{u}_R + \alpha k_0(u_R - u_n) + (1 - \alpha)k_0 u_y z(t) = 0 \end{cases} \quad (24)$$

where dots refer to time differentiation. We assume the following harmonic solution for displacements:

$$\begin{aligned} u_n &= \tilde{u}_n e^{i\omega t} \\ u_R &= \tilde{u}_R e^{i\omega t} \end{aligned} \quad (25)$$

where \tilde{u}_n and \tilde{u}_R are displacement amplitudes. In addition, the Floquet-Bloch theorem can be applied as

$$\begin{aligned} u_{n+1} &= \tilde{u}_n e^{i\mu} \\ u_{n-1} &= \tilde{u}_n e^{-i\mu} \end{aligned} \quad (26)$$

where $\mu = \kappa d$ defines the so-called propagation constant based on the wavenumber κ and the unit cell length d . Thus, the application of the ELT by means of Eqs. (12) and (18) and the conditions of Eqs. (25)–(26) to the system of Eq. (24) entails the following:

$$\begin{cases} \left[-\omega^2 m_n + 2k_n + 2i\omega c_n + \alpha k_0 - \frac{i\omega}{i\omega + k_{eq}} c_{eq}(1 - \alpha)k_0 u_y \right] u_n + \left[-\alpha k_0 + \frac{i\omega}{i\omega + k_{eq}} c_{eq}(1 - \alpha)k_0 u_y \right] u_R - (k_n + i\omega c_n)(e^{-i\mu} + e^{i\mu})u_n = 0 \\ u_R = \frac{\alpha k_0 - \frac{i\omega}{i\omega + k_{eq}} c_{eq}(1 - \alpha)k_0 u_y}{-\omega^2 m_n + \alpha k_0 - \frac{i\omega}{i\omega + k_{eq}} c_{eq}(1 - \alpha)k_0 u_y} u_n \end{cases} \quad (27)$$

The substitution of u_R into the first equation of Eq. (27) leads to the following dispersion relation:

$$\mu = \arccos \left(\frac{-\omega^2 m_n + 2k_n + 2i\omega c_n + \alpha k_0 - \frac{i\omega}{i\omega + k_{eq}} c_{eq}(1 - \alpha)k_0 u_y + \frac{\left[-\alpha^2 k_0^2 + 2\alpha k_0 \frac{i\omega}{i\omega + k_{eq}} c_{eq}(1 - \alpha)k_0 u_y - \left(\frac{i\omega}{i\omega + k_{eq}} c_{eq}(1 - \alpha)k_0 u_y \right)^2 \right]}{-\omega^2 m_n + \alpha k_0 - \frac{i\omega}{i\omega + k_{eq}} c_{eq}(1 - \alpha)k_0 u_y}}{2(k_n + i\omega c_n)} \right) \quad (28)$$

in the $(\mu - \omega)$ plane.

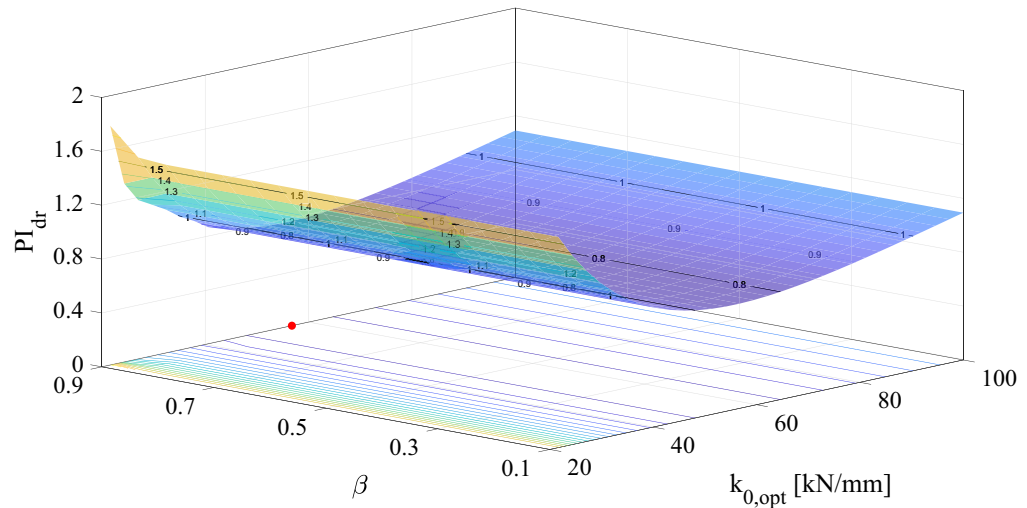


Figure 8. Optimal surface for the linearized CMS.

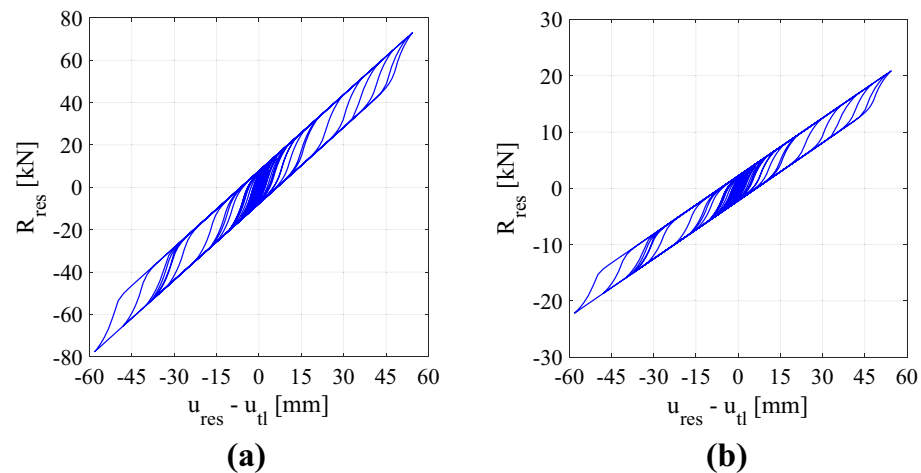


Figure 9. Hysteretic loops of the one-layer CMS hysteretic damper for $A = 1$, $\beta = 0.9$ and $\gamma = 0.1$. The resonators are equipped with the (a) optimal and (b) minimum numbers of wire ropes.

Results

Optimization and time-history analysis results. The optimization and time history analyses based on the methods discussed at length in the previous section are presented and discussed herein. We set n , α and u_y based on the properties described in Table 1, and we search for the optimal values of k , β and γ with the constraints²⁹ $A = 1$ and $\beta + \gamma = 1$. The results of the optimization process based on the index PI_{dr} introduced in Eq. (20) are depicted in Fig. 8 for the CMS model. The minimum value of $PI_{dr} = 0.78$, i.e., the red point on the $\beta - k_{0,opt}$ plane, corresponds to $k_{0,opt} = 56.8$ KN/mm and $\beta^{opt} = 0.9$. β and γ quantify the dissipation characteristics of wire ropes, and with $\beta + \gamma = 1$, $\gamma^{opt} = 0.1$. Notably, $k_{0,opt}$ corresponds to the horizontal stiffness of a single resonator of the metafoundation. Similar values can be obtained by means of the index PI_{acc} .

To test the performance of the metafoundation-tank coupled system, THAs are carried out considering the hysteretic responses of the devices in agreement with Eq. (5). Figure 9 shows the hysteretic loops of a single wire rope when the CMS is subjected to one of the 12 accelerograms listed in Table 2. The term u_{res} represents the displacement of the generic resonator w.r.t. u_{tl} , i.e., the displacement of the top of the metafoundation. Figure 9a refers to the optimized system where 42 wire ropes per resonator are needed. Conversely, Fig. 9b refers to the system provided with the minimum number of wire ropes required to support a resonator, i.e., 16 wire ropes.

To appreciate the performance of the optimized finite lattice metafoundation, Fig. 10 depicts both the maximum and the median parameter values of the nonlinear foundation-tank coupled system w.r.t. the fixed-base solution when subjected to the 12 seismic records listed in Table 2. The maximum values of the base shear V , absolute acceleration a and interstorey drift d of the impulsive mass are reported. Nonlinear devices are characterized by β and γ equal to 0.9 and 0.1, respectively. The favourable performance of the metafoundation, which

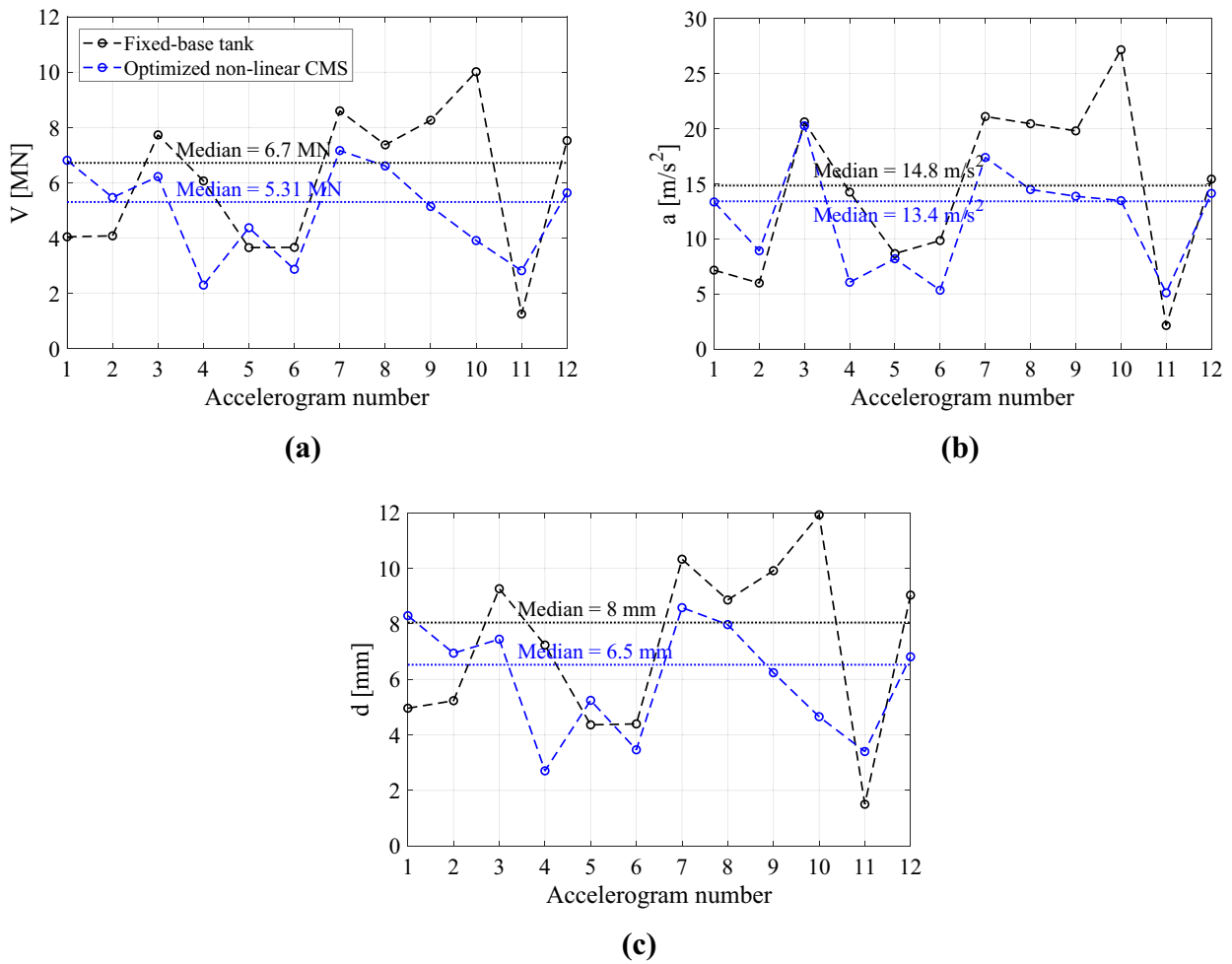


Figure 10. Maximum and median values of the (a) base shear, (b) absolute acceleration and (c) interstorey drift of the optimized nonlinear CMS w.r.t. the fixed-base tank for each accelerogram listed in Table 2.

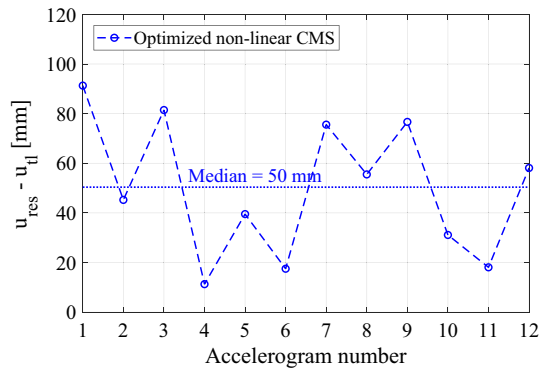


Figure 11. Maximum and median values of wire ropes for the optimized nonlinear CMS for each time history.

achieves reductions of approximately 21%, 10% and 19% in V , a , and d , respectively, w.r.t. the fixed-base case, is evident.

Finally, Fig. 11 shows the maximum and median values of the wire rope displacements in the optimized nonlinear CMS relevant to each time history. The maximum displacements reach approximately 90 mm with a median equal to 50 mm. These demand values are compatible with the capacities of standard wire ropes.

Dispersion curves of the linearized periodic system. For the sake of completeness, it is worthwhile to examine some wave propagation properties of the decoupled metafoundation depicted in Fig. 7a and modelled

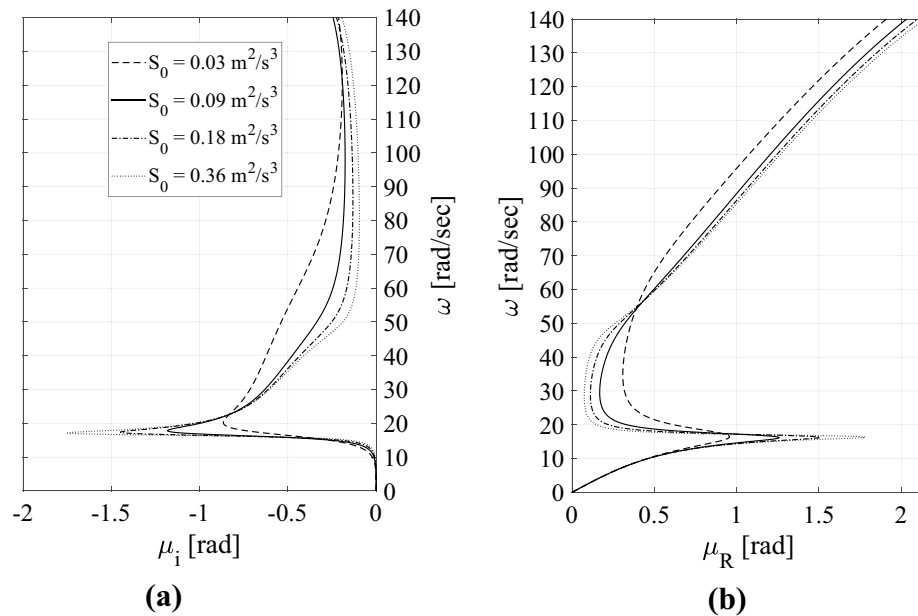


Figure 12. Periodic metafoundation dispersion curves: **(a)** imaginary component of μ ; **(b)** real component of μ .

as a periodic system in Fig. 7b. We rely on the ELT applied to nonlinear devices so that we are able to trace the mode shape families, i.e., the dispersion curves or band structures, defined by means of wavelengths—inversely, wavenumbers—and frequencies. As the linearized hysteretic system exhibits a significant amount of damping (see Eqs. (16) and (17)), the damped periodic materials can be characterized by means of (1) complex wavenumbers as a function of real frequencies and (2) complex frequencies as a function of real wavenumbers. We adopt the former methodology, where the dispersion relationships are obtained with Eq. (28) in terms of $\mu(\omega)$. This condition corresponds to a harmonic wave motion where a driving frequency ω is prescribed. The values of the propagation constant $\mu(\omega)$ are all complex due to the presence of damping. The relevant dispersion relationships representative of the periodic metafoundation depicted in Fig. 7b are shown in Fig. 12. The relationships are expressed by real values of μ corresponding to the propagative index of waves, while the imaginary components of μ , often called the attenuation constant, define the spatial decay of the amplitude as the wave progresses through the lattice.

Each dispersion curve shown in Fig. 12 is associated with a different value of k_{eq} that, due to the linearization process, depends on the input PSD S_0 . Standard ELT results^{30,31} show that an increase in S_0 from 0.03 to 0.36 m^2/s^3 entails an increase in k_{eq} —83, 177, 273 and 410—whilst c_{eq} remains essentially unchanged and equal to $c_{eq} = -269$. As shown by Spanos and Giaralis³³, k_{eq} and c_{eq} are derived from a third-order ELT whose values do not correspond to any particular mechanical system; hence, their physical significance is limited. Conversely, if we rely on a second-order statistical linearization scheme³³ governed by the linearization parameters ζ_{eq} and ω_{eq} , this leads to a trend where an increase in S_0 corresponds to a reduction in ω_{eq} , as understood from Fig. 12a. Note that for the highest value of S_0 , i.e., almost an undamped-like structure, the curve tends to create a band-gap. In that area, the μ_i values are higher for curves with less damping. Finally, with regard to waves travelling at frequencies that belong to the passband of μ_R , higher damping values entail greater spatial wave attenuation.

Numerical investigation of the periodic system. In contrast to the previous subsection, where we considered a linearized periodic system, in this section we carry out numerical simulations on the metafoundation's periodic configuration depicted in Fig. 7b; thus, we do not make any assumptions about the nonlinearities involved. The system is excited by a time-harmonic displacement A_0 applied to the bottom layer. The output response A is read from the top layer. The boundary condition of the system of masses is free-free, and since the system is not excited by a force, rigid-body motion is avoided. The frequency response function (FRF) is then evaluated as

$$FRF = 20 \log_{10} \frac{A}{A_0} \quad (29)$$

where A is the maximum amplitude of the steady-state response and A_0 is the amplitude of the harmonic excitation. The resulting wave transmittances are plotted in Fig. 13.

The FRFs of Fig. 13 are clearly amplitude dependent because the system is nonlinear. However, the wave transmittances in Fig. 13a for low frequencies show that the modal resonances do not depend strongly on the amplitude excitation. This is clearly confirmed by the linearized band structure observed in Fig. 12, where the acoustic branch appears to be identical for each S_0 . Nevertheless, the identification of an optical branch is simpler for high amplitudes, i.e., $A_0 = 25$ cm; in fact, the presence of resonance points becomes evident.

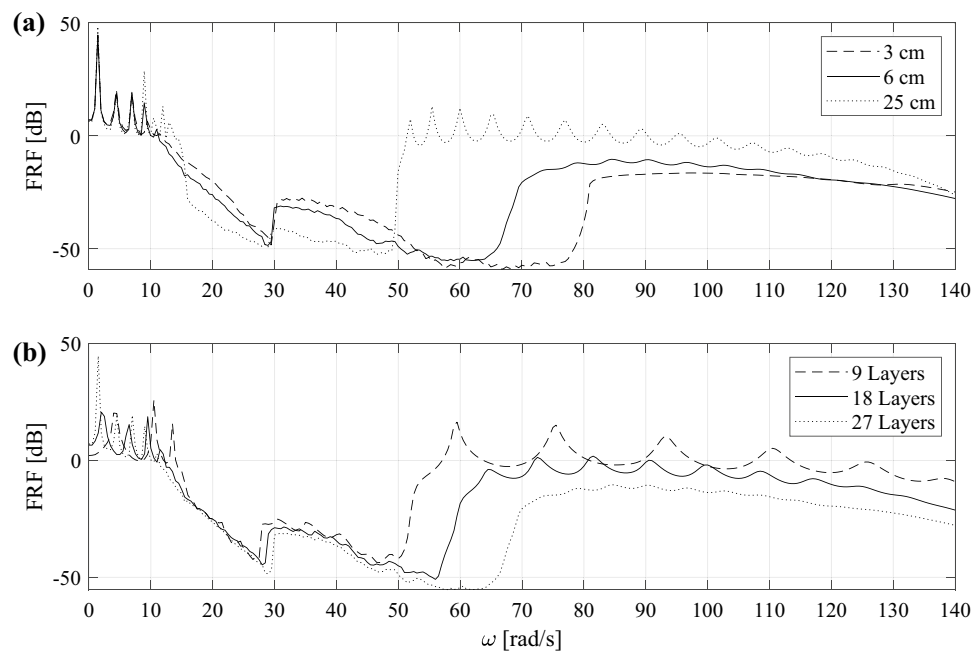


Figure 13. Numerical FRFs of a periodic finite lattice: (a) FRF for several input amplitudes A_0 for 27 layers; (b) FRF for several layers for $A_0 = 6$ cm.

We can also identify a strong attenuation zone comparable to the band gap. The width of the band gap varies with the displacement amplitude. A wide and deep band gap can be observed under small-amplitude excitations, whereas the width and depth of the band gap are reduced by increasing the input amplitude. This leads to a worse wave attenuation performance of the hysteretic system under high-amplitude vibrations. The performance of the periodic hysteretic system can also be evaluated by means of Fig. 13b for $A_0 = 6$ cm. It is clear that the performance level increases in terms of the width and depth of the band gap as the system is characterized by more layers. Moreover, it is worth noting that both FRFs identify an attenuation zone accurately predicted by the linearized dispersion curves of Fig. 12. In fact, the trend of the imaginary components of μ is centred at the resonator's linearized frequency $\omega_R = (\alpha k_0 / m_R)^{1/2} = 16,9$ rad/s. Figure 13 consistently shows that for frequencies ranging from approximately 15 to 20 rad/sec, the FRF starts to decrease. Finally, note that the stiffness αk_0 corresponds to the slope of the hardening branch of the Bouc–Wen model in Eq. (7).

Discussion

The objective of this work was to conceive a metafoundation bearing oil storage tanks capable of inheriting the filter properties of finite lattice phononic structures. More precisely, the vibrations in the frequency regime induced by seismic records are attenuated by the favourable properties of coupled hysteretic devices and resonators embedded in the metafoundation. The metafoundation is composed of massive vibrating concrete blocks that are coupled to the slabs by means of fully nonlinear hysteretic devices. Moreover, to achieve cost savings, the foundation is constituted by a single layer of resonators.

To identify the effective properties of nonlinear hysteretic devices in terms of stiffness and equivalent damping, an optimization procedure was carried out by minimizing two dimensionless performance indices based on the variances of interstorey displacement of the impulsive mass and of the relevant absolute acceleration. Because the optimization procedure has to be carried out in the frequency domain for linear time-invariant systems subjected to stationary seismic records, we applied the stochastic linearization technique¹⁹ to the nonlinear hysteretic devices embedded in the metafoundation. As a result, the optimized metafoundation-tank coupled system performed well when subjected to natural seismic records carried out in the time domain. In addition, we determined the dispersion relations for the periodic linearized spring–mass chain, see Fig. 7b, which clearly depends on the PSD S_0 amplitude. As a result, the maximum attenuation rate, based on the propagation constant depicted in Fig. 12a, increases with an increase in S_0 and a decrease in the equivalent damping ζ_{eq} in the resonators.

Furthermore, we investigated the nonlinear response of the periodic metafoundation by means of numerical FRFs. The results confirm the reliability of the dispersion analysis subsequent to applying the equivalent linearization technique. In fact, a strong attenuation zone in the FRF is located in the frequency range where the dispersion curves indicate very high values of the imaginary propagation constant μ_i .

The results achieved herein reveal a promising application of finite lattice metafoundations to large systems subjected to strong seismic excitations. In addition, this work paves some ways: (1) the application of stochastic linearization to a finite lattice allows the metafoundation-tank coupled nonlinear system to be optimized while capturing the variability of the seismic input, and (2) the use of simple hysteretic devices such as wire ropes

permits the 3D motion of massive resonators and reflect the great effectiveness and potential of these devices as vibration mitigation tools.

Ultimately, the validation of these results by means of the 3D physical characterization of hysteretic devices as well as the analysis of nonlinear wave mechanisms through nonlinear spatial analyses deserve further study.

Received: 23 December 2020; Accepted: 19 April 2021

Published online: 06 May 2021

References

1. Calhoun, S. J., Tehrani, M. H. & Harvey, P. S. On the performance of double rolling isolation systems. *J. Sound Vib.* **449**, 330–348 (2019).
2. La Salandra, V., Wenzel, M., Bursi, O. S., Carta, G. & Movchan, A. B. Conception of a 3D metamaterial-based foundation for static and seismic protection of fuel storage tanks. *Front. Mater.* **4**, 30 (2017).
3. Cheng, Z. B. & Shi, Z. F. Composite periodic foundation and its application for seismic isolation. *Earthq. Eng. Struct. Dyn.* **47**(4), 925–944 (2018).
4. Casablanca, O. *et al.* Seismic isolation of buildings using composite foundations based on metamaterials. *J. Appl. Phys.* **123**(17), 174903 (2018).
5. Schellenberg, A. H., Sarebanha, A., Schoettler, M. J., Mosqueda, G. & Benzoni, G. Hybrid simulation of seismic isolation systems applied to an APR-1400 nuclear power plant. PEER Reports, Headquarters at the University of California (2015).
6. Basone, F., Wenzel, M., Bursi, O. S. & Fossetti, M. Finite locally resonant metafoundations for the seismic protection of fuel storage tanks. *Earthq. Eng. Struct. Dyn.* **48**(2), 232–252 (2019).
7. Carta, G., Movchan, A. B., Argani, L. P. & Bursi, O. S. Quasi-periodicity and multi-scale resonators for the reduction of seismic vibrations in fluid-solid systems. *Int. J. Eng. Sci.* **109**, 216–239 (2016).
8. Ministero delle Infrastrutture e dei Trasporti. Aggiornamento delle 'Norme tecniche per le costruzioni' (in Italian) pp. 1–198 (2018).
9. Paolacci, F. & Giannini, R. Study of the effectiveness of steel cable dampers for the seismic protections of electrical equipment. *World Conf. Earthq. Eng.* (2008).
10. Alessandri, S., Giannini, R., Paolacci, F. & Malena, M. Seismic retrofitting of an HV circuit breaker using base isolation with wire ropes. Part I: preliminary tests and analyses. *Eng. Struct.* **98**, 251–262 (2015).
11. Balaji, P. S., Moussa, L., Rahman, M. E. & Ho, L. H. An analytical study on the static vertical stiffness of wire rope isolators. *J. Mech. Sci. Technol.* **30**(1), 287–295 (2016).
12. Wen, Y. Method for random vibration of hysteretic systems. *J. Eng. Mech. Div. Proc. ASCE* **102**, 249–263 (1976).
13. Zhou, W. J., Li, X. P., Wang, Y. S., Chen, W. Q. & Huang, G. L. Spectro-spatial analysis of wave packet propagation in nonlinear acoustic metamaterials. *J. Sound Vib.* **413**, 250–269 (2018).
14. Zivieri, R., Garesci, F., Azzèrboni, B., Chiappini, M. & Finocchio, G. Nonlinear dispersion relation in anharmonic periodic mass-spring and mass-in-mass systems. *J. Sound Vib.* **462**, 114929 (2019).
15. Chakraborty, G. & Mallik, A. K. Dynamics of a weakly non-linear periodic chain. *Int. J. Non-linear Mech.* **36**(2), 375–389 (2001).
16. Fang, X., Wen, J., Bonello, B., Yin, J. & Yu, D. Ultra-low and ultra-broad-band nonlinear acoustic metamaterials. *Nat. Commun.* **8**(1), 1288 (2017).
17. Zega, V., Silva, P. B., Geers, M. G. D. & Kouznetsova, V. G. Experimental proof of emergent subharmonic attenuation zones in a nonlinear locally resonant metamaterial. *Sci. Rep.* **10**(1), 12041 (2020).
18. Gupta, V., Adhikari, S. & Bhattacharya, B. Exploring the dynamics of hourglass shaped lattice metastructures. *Sci. Rep.* **10**(1), 20943 (2020).
19. Caughey, T. K. Equivalent linearization techniques. *J. Acoust. Soc. Am.* **35**(11), 1706–1711 (1963).
20. Kumar, A., Saha, S. K. & Matsagar, V. A. Stochastic response analysis of elastic and inelastic systems with uncertain parameters under random impulse loading. *J. Sound Vib.* **461**, 114899 (2019).
21. Socha, L. & Pawleta, M. Are statistical linearization and standard equivalent linearization the same methods in the analysis of stochastic dynamic systems? *J. Sound Vib.* **248**(2), 387–394 (2001).
22. Malhotra, P. K., Wenk, T. & Wieland, M. Simple procedure for seismic analysis of liquid-storage tanks. *Struct. Eng. Int.* **10**(3), 197–201 (2000).
23. Housner, G. W. The dynamic behavior of water tanks. *Bull. Seismol. Soc. Am.* **53**, 381–387 (1963).
24. Kanai, K. Semi-empirical formula for the seismic characteristics of the ground. *Bull. Earthq. Res. Inst.* **35**, 309–324 (1975).
25. Clough, R. W., Penzien, J. & Griffin, D. S. Dynamics of structures. *J. Appl. Mech.* **44**(2), 366–366 (1977).
26. O'Callahan, R. R. J. & Avitabile, P. System equivalent reduction expansion process (SEREP). In *Proc. 7th Int. Modal Anal. Conf. Las Vegas* 29–37 (1989).
27. Franchini, A., Bursi, O. S., Basone, F. & Sun, F. Finite locally resonant metafoundations for the protection of slender storage tanks against vertical ground accelerations. *Smart Mater. Struct.* **29**(5), 055017 (2020).
28. Bonelli, A. & Bursi, O. S. Generalized- α methods for seismic structural testing. *Earthq. Eng. Struct. Dyn.* **33**(10), 1067–1102 (2004).
29. Constantinou, M. C. & Adnane, M. A. Dynamics of soil-based-isolated-structure systems: evaluation of two models for yielding systems. *Report to the National Science Foundation*. Dept. of civil Engng. Drexel Univ. (1987).
30. Maldonado, G. O., Singh, M. P., Heller, R. A. & Frederick, D. Stochastic response of single degree of freedom hysteretic oscillators. *Technical Report of Research Supported by The National Science Foundation Under Grant Number CEE-8412830* (1987).
31. Spanos, P. D. & Roberts, J. B. *Random Vibration and Statistical Linearization* (Wiley, 1990).
32. Bartels, R. H. & Stewart, G. W. Solution of the matrix equation $AX + XB = C$. *Commun. ACM* **15**(9), 820–826 (1972).
33. Spanos, P. D. & Giaralis, A. Third-order statistical linearization-based approach to derive equivalent linear properties of bilinear hysteretic systems for seismic response spectrum analysis. *Struct. Saf.* **44**, 59–69 (2013).

Acknowledgements

This work received support from the European Union's Horizon 2020 research and innovation program under the Marie Skłodowska-Curie Grant agreement no. INSPIRE-813424 for the third and fourth authors and the Italian Ministry of Education, University and Research (MIUR) in the frame of the 'Departments of Excellence' (Grant L 232/2016) for the remaining authors.

Author contributions

O.S.B and F.B. developed the initial concepts and outlined the research. F.B. performed the theoretical calculations, conducted the numerical simulations and verified the relevant results. F.A. performed the theoretical

dispersion analysis and conducted the relevant numerical simulations. F.B. and F.A. prepared all figures and drafted the manuscript. O.S.B. and G.F. heavily contributed to the seismic design and analysis. The authors jointly discussed the results and revised the manuscript.

Competing interests

The authors declare no competing interests.

Additional information

Supplementary Information The online version contains supplementary material available at <https://doi.org/10.1038/s41598-021-88984-0>.

Correspondence and requests for materials should be addressed to O.S.B.

Reprints and permissions information is available at www.nature.com/reprints.

Publisher's note Springer Nature remains neutral with regard to jurisdictional claims in published maps and institutional affiliations.



Open Access This article is licensed under a Creative Commons Attribution 4.0 International License, which permits use, sharing, adaptation, distribution and reproduction in any medium or format, as long as you give appropriate credit to the original author(s) and the source, provide a link to the Creative Commons licence, and indicate if changes were made. The images or other third party material in this article are included in the article's Creative Commons licence, unless indicated otherwise in a credit line to the material. If material is not included in the article's Creative Commons licence and your intended use is not permitted by statutory regulation or exceeds the permitted use, you will need to obtain permission directly from the copyright holder. To view a copy of this licence, visit <http://creativecommons.org/licenses/by/4.0/>.

© The Author(s) 2021